Sensitivity analysis on miniaturize pulse tube boundary layer losses

IOP Conf. Series: Materials Science and Engineering **755** (2020) 012014 doi:10.1088/1757-899X/755/1/012014

Sensitivity analysis on miniaturize pulse tube boundary layer losses

Ali Ghavami[1], Carl Kirkconnell[2] and S Mostafa Ghiaasiaan[1]
[1]Georgia Institute of Technology, G.W. Woodruff School of Mechanical Engineering, Atlanta, GA, USA 30332;
[2]West Coast Solutions, 17682 Gothard Street, Suite 201, Huntington Beach, CA, USA 92647

ali.ghavami@gatech.edu

Abstract. Miniaturized cryocooler systems are among the key components of state-of-art infrared sensing small satellites (SmallSats). To achieve small size, these cryocoolers need to operate at high frequencies, e.g., 200 to 300 Hz range. High frequency leads to lower compression and expansion swept volumes and hence a smaller cryocooler. Previously we showed that pulse tube cryocoolers have high boundary layer losses for small size pulse tube diameters, which results in low thermodynamic efficiency. In this follow-up study we present a sensitivity analysis on the pulse tube boundary layer losses and investigate the effects of the bounding temperatures, pulse tube aspect ratio, operating frequency and pulse tube diameter. Computational fluid dynamics (CFD) is used for this sensitivity analysis. The results allow us to find the threshold conditions beyond which a miniature pulse tube cryocooler can no longer be effective for use at high frequencies.

1. Introduction

Miniaturized cryocoolers are among the key components of the state-of-the-art infrared sensors used on small satellites (SmallSats). The main application of these SmallSats is taking night-time and multispectral images of earth and other planetary bodies.

Operating at high frequency is an essential condition for small size cryocoolers. Compression and expansion swept volumes are smaller in high frequency systems and consequently moving mechanisms as well as other components of these cryocoolers need to be miniaturized. Miniature Stirling cryocoolers are chosen over miniature pulse tube coolers because of their proven better performance at high frequency and the temperature range 300 K to 80 K [1, 2]. Miniaturization in pulse tubes that work at high frequency leads to high boundary layer losses and a drastic reduction of thermal efficiency [3]. However, miniature Stirling cryocoolers are susceptible to shuttle loss heat transfer, which under certain conditions can be very important. The shuttle heat transfer loss needs to be considered and minimized during the design of Stirling cryocoolers [4]. The solid model concept for a single piston Stirling compressor cryocooler with a passive expander is shown in Figure 1. The component sizing depicted in this figure is based on thermodynamic model optimization at 300 Hz operating frequency and 80 K cold end temperature. Detailed information about the cryocooler can be found in [5].

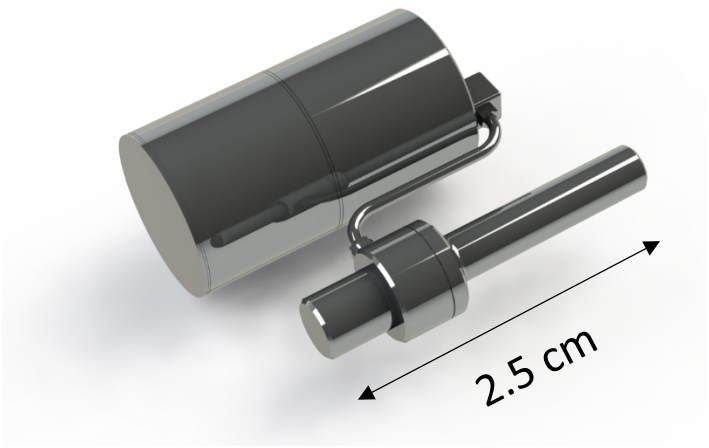

Figure 1. Solid model concept design for the SmallSat Stirling Cryocooler [5].

In a previous work [3], it was shown that boundary layer losses increase as diameter of a pulse tube decreases from meso-scale 10 mm down to 1 mm at 300 Hz, and this leads to very low thermodynamic efficiency at 1 mm diameter. In this follow up study, computational fluid dynamics (CFD) is utilized to conduct sensitivity analysis on pulse tubes to investigate the effect of geometric parameters and operating conditions on boundary layer losses. For this analysis, the effects of bounding temperature, pulse tube aspect ratio, and frequency are investigated. The results provide the threshold condition beyond which the miniature pulse tube has high boundary losses and can no longer be used for working at high frequency in single stage and multistage cryocoolers. Beyond this threshold, single stage Stirling or hybrid Stirling/pulse tube cryocoolers can be used instead of miniature pulse tube cryocoolers. Losses in the regenerator and other cryocooler components as well as shuttle loss heat transfer are not addressed in this analysis.

2. Geometric configuration and model assumptions

Figure 2 shows the computational domain and boundary conditions in this study, and Table 1 summarizes the model parameters. The basis of model parameters comes from earlier paper [3]. CFD analysis is performed on this pulse tube expander to examine the dependence of the boundary layer losses on operating conditions and geometric parameters. This work is a follow up of previous work [3], where only diameter was reduced from 10 mm to 1mm while the aspect ratio of the pulse tube and its operating conditions remained constant. It was shown that as diameter shrinks, the boundary layer losses becomes stronger, which leads to lower efficiency.

In our previous work [3], we analyzed the same system for a fixed frequency of 300 Hz, bounding temperatures of 80 K to 300 K, and a fixed aspect ratio of 10. In this sensitivity analysis these parameters are all varied for three pulse tubes with diameters of 7, 4, and 1 mm. In each set of simulations, only one parameter is varied while other variables remain constant. Two sets of bounding temperatures, 300K-80K and 80K-40K, are used. The first set of temperature, 300K-80K, investigates the boundary layer losses and applicability of pulse tube refrigeration in the first stage of a typical two-stage cryocooler, while the second set, 80K-40K, is representative of a typical second stage of a cryocooler. The operating frequency varies from 175 Hz to 300 Hz and the aspect ratio of the pulse tube is varied from 6 to 14.

The cold and hot heat exchangers which are located on the two ends of the pulse tube depicted in Figure 2 are arbitrary and are meant to provide isothermal and uniform flow entering the pulse tube. The length of these heat exchangers is 0.3 times the length of the pulse tube. The heat exchanger inertial resistance, which represents inertial loss in porous media, and porosity are set to $8147 m^{-1}$ and 0.68, respectively, and are held constant for all cases.

The inlet and outlet are subject to oscillating mass flow rates with a fixed phase angle of 30 degrees (cold end leading). Details of the mass flow rate amplitude at both cold and hot ends are described in the next section. The temperature of the gas and the heat exchanger wall at the cold end are set to T_{cold}, while the temperature of the gas and the heat exchanger wall at the hot end are set to T_{hot}. The wall of the pulse tube is assumed to be insulated and have zero heat flux. The system is axisymmetric.

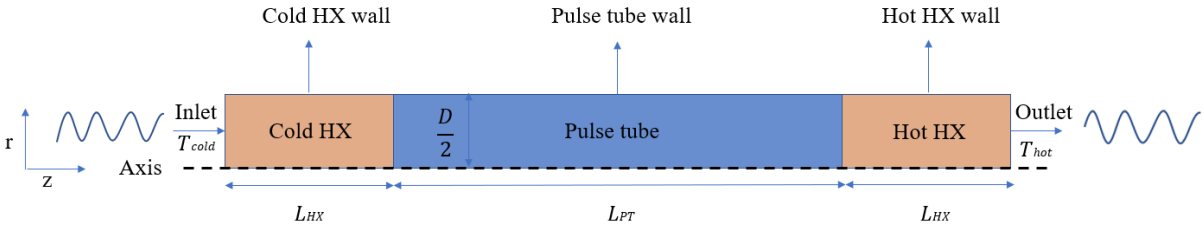

Figure 2. Computational domain with boundaries.

Table 1. Model parameters.

Model parameter	Value
Working gas	Helium
Frequency (f)	Varies between 175 – 300 Hz (sinusoid)
Cold end temperature (T_{cold})	Varies between 80 – 190 K at T_{hot}= 300 K, Varies between 40 – 60 K at T_{hot}= 80 K
Hot end temperature (T_{hot})	Varies between 300 – 190 K at T_{cold}= 80 K, Varies between 80 – 60 K at T_{cold}= 40 K
Mean pressure (P_{mean})	1.54 – 1.59 MPa (derived after running simulation, not specified explicitly)
Cold and hot mass flow rate phase angle (θ)	30° cold end leading
Pulse tube diameter (D)	1, 4, 7 mm
Pulse tube length (L_{PT})	Derived based on aspect ratio
Pulse tube aspect ratio (L_{PT}/ D)	Varies between 6 – 14
Heat exchanger diameters	D
Heat exchanger lengths (L_{HX})	$0.3L_{PT}$
Heat exchanger viscous resistance	7.435×10^{8} m^{-2}
Heat exchanger inertial resistance	8147 m^{-1}
Heat exchanger porosity	0.68

3. Theory and method of solution

By assuming incompressible and Newtonian fluid, the continuity, momentum and energy equations which are numerically solved are as follows:

$$\frac{\partial u_j}{\partial x_j} = 0 \tag{1}$$

$$\frac{\partial u_i}{\partial t} + \frac{\partial}{\partial x_j} u_j u_i = - \frac{1}{\rho}\frac{\partial P}{\partial x_i} + \frac{\partial}{\partial x_j} \nu \left(\frac{\partial u_i}{\partial x_j} + \frac{\partial u_j}{\partial x_i} \right) \tag{2}$$

$$\rho c \left(\frac{\partial T}{\partial t} + \frac{\partial}{\partial x_j} u_j T \right) = \frac{\partial}{\partial x_j} \left(k \frac{\partial T}{\partial x_j} \right) \tag{3}$$

where ν, ρ, c, and k are kinematic viscosity, density, specific heat, and conductivity of the fluid, respectively. Temperature dependent properties at P_{mean}, which is the average working pressure in the

pulse tube, are used for other thermodynamic parameters. Temperature dependent properties are extracted from Engineering Equation Solver (EES) software [6] for the 300K-40K temperature rage, at P_{mean}. For convenience, however, polynomial regression is fitted to these data and the forthcoming equations for density, dynamic viscosity, heat capacity and conductivity are derived:

$$\rho\left(\frac{kg}{m^3}\right) = -2\times10^{-6}T^3 + 0.0013T^2 - 0.2944T + 25.43 \tag{4}$$

$$\mu\left(\frac{kg}{m.s}\right) = 5\times10^{-8}T + 4\times10^{-6} \tag{5}$$

$$c\left(\frac{kJ}{kg.K}\right) = -3\times10^{-8}T^3 + 2\times10^{-5}T^2 - 0.0041T + 5.459 \tag{6}$$

$$k\left(\frac{W}{m.K}\right) = 0.0004T + 0.0313 \tag{7}$$

Mass flow rate amplitude at both cold and hot ends of the pulse tube are calculated based on gas displacement through the pulse tube in each half cycle. In typical pulse tube cryocoolers, the gas volume displaced in a half cycle is approximately 25% of the total volume of the pulse tube. The amplitude of the mass flow rate can be normalized with respect to pulse tube size mathematically by [3]:

$$dV = dV_c = dV_h = 0.25V_{PT} = 0.25\frac{\pi D^2}{4}L_{PT} \tag{8}$$

$$dM_c = \frac{dV \times P_{mean}}{R \times T_{cold}}, \qquad dM_h = \frac{dV \times P_{mean}}{R \times T_{hot}} \tag{9}$$

$$|\dot{m}_{cold}| = \sqrt{2}\frac{dM_c}{dt} = \sqrt{2} \times dM_c \times 2f, \qquad |\dot{m}_{hot}| = \sqrt{2}\frac{dM_h}{dt} = \sqrt{2} \times dM_h \times 2f \tag{10}$$

where R is ideal gas constant.

In evaluating the effect of miniaturization on cooling performance, the efficiency is defined based on the ratio between cycle average enthalpy transport rate and the input PV power in each cycle:

$$\eta = \frac{<\dot{H}>}{<P\dot{V}>} \tag{11}$$

The cycle average enthalpy transport rate and input PV power can be calculated, respectively, from:

$$<\dot{H}> = \frac{\int_{cycle}\left(\int_0^{D/2}\rho v_{axial}\left(h + \frac{1}{2}|v|^2\right)2\pi r dr\right)dt}{t_{cycle}} \tag{12}$$

$$<P\dot{V}> = \frac{1}{2}RT_{cold}\left(\frac{P_{amp}}{P_{mean}}\right)|\dot{m}_{cold}|cos\theta \tag{13}$$

where t_{cycle} is period time of a cycle, v_{axial} is flow velocity in the axial direction, and P_{amp} is pressure amplitude ($P_{max} - P_{mean}$) in pulse tube.

4. Numerical solution procedure

ANSYS Fluent [7] is used for performing this sensitivity analysis and solving equations 1-3. The oscillating mass flow rate is applied at the inlet and outlet of computational domain by the aid of a user define function (UDF) in Fluent, according to:

$$\dot{m}_{inlet} = |\dot{m}_{cold}|sin(2\pi ft), \quad \dot{m}_{outlet} = |\dot{m}_{hot}|sin(2\pi ft - \theta) \tag{14}$$

where $|\dot{m}_{cold}|$ and $|\dot{m}_{hot}|$ are calculated from equation 10. The UDF code is developed in C++ [8].

Simulations for grid size effect showed that grid independent solutions can be achieved with 640 axial elements (120 elements for each heat exchanger and 400 elements for pulse tube) and 50 radial elements. Using significantly finer grids led to less than 0.8% change in cycle average enthalpy transport rate across the pulse tube. To capture the boundary layer effects, finer mesh is used at the wall by defining a bias factor of 2.25 in radial direction whereby Δr of centerline elements (elements at the axis)

are 2.25 times of elements at the wall. This mesh is shown in Figure 3 for a portion of computational domain.

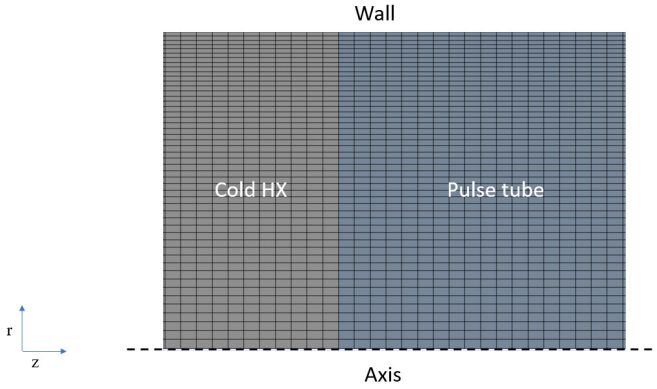

Figure 3. Mesh generation on the portion of pulse tube and cold heat exchanger.

The analysis is two-dimensional and axisymmetric. Pressure based solver with SIMPLE algorithm is used to solve pressure-velocity coupling. For discretization of governing equations, the standard second order method for pressure, second order upwind scheme for momentum and energy equations, and least squares method for gradients is implemented by finite volume technique. For convergence criteria, the residual is set to 10^{-6} for continuity and momentum equations, and 10^{-13} for energy equation. The analysis is transient and the time step is set to 1.66×10^{-5}. The periodic steady state solution, where the cyclic variation of all parameters is repeated identically, was achieved after 100 cycles for all simulation cases. Post processing of results was performed by MATLAB [9] and Tecplot [10].

5. Results and discussion

Figure 4 illustrates the convergence of the simulations. Cases with different diameters at T_{hot}= 300 K, T_{cold}= 80 K and f= 200 Hz are shown in Figure 4 as examples. Figure 4 (a) shows that periodic steady state solution is achieved after 100 cycles based on the cycle average total enthalpy flux at the middle of the pulse tube. Figure 4 (b) shows that the cycle average total enthalpy flux reaches a constant value along the entire pulse tube once periodic steady state has been achieved. The axial position in the pulse tube is divided by L_{PT} for the sake of normalization.

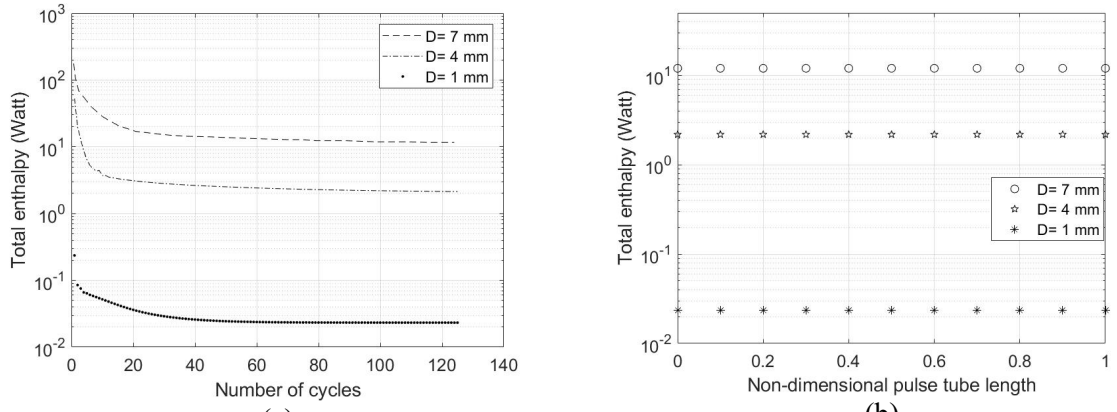

Figure 4. Convergence of results for cases with T_{hot}= 300 K, T_{cold}= 80 K, and f= 200 Hz, (a) the effect of number of cycles on convergence of cycle average total enthalpy flux at the middle of the pulse tube, (b) cycle average total enthalpy flux throughout the length of the pulse tube at steady periodic conditions (100^{th} cycle).

Figure 5 illustrates the dependence of the boundary layer on pulse tube size for f= 300 Hz and a constant pulse tube aspect ratio of 10, for different bounding temperatures. The cold and hot heat exchangers are not shown and the diameter to length ratio has been multiplied by 4 for better visualization of boundary effects. The top edge is wall and the bottom edge is axis in each contour. These contours are at 1/4 cycle where the mass flow rate is maximum at the cold end. As diameter decreases, radial variation of temperature as well as mixing in flow direction (left to right) increases which leads to more boundary losses. Also, comparing Figures 5 (a) and 5 (b) indicates significantly less steep temperature gradients at the wall for the T_{cold}= 40 K and T_{hot}= 80 K cases. This is shown quantitatively in Figure 6 where the standard deviations of the distribution of fluid temperatures over the cross-section of the pulse tube at the middle of the pulse tube during a cycle are plotted. Larger values of standard deviation indicate more deviation from one-dimensional flow, hence more boundary layer losses.

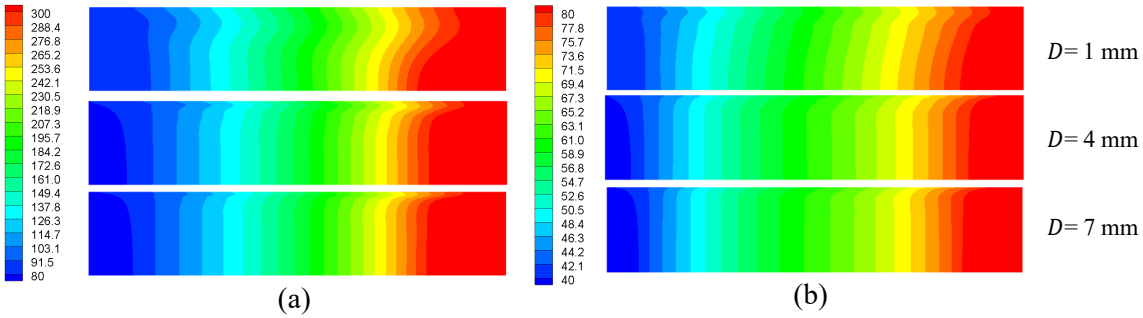

Figure 5. Temperature contours (K) at 1/4 cycle for f= 300 Hz with a pulse tube aspect ratio of 10, (a) T_{cold}= 80 K and T_{hot}= 300 K, (b) T_{cold}= 40 K and T_{hot}= 80 K.

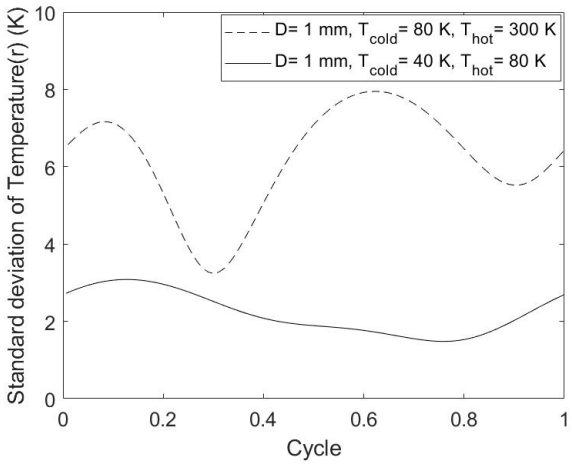

Figure 6. Standard deviation of the distribution of temperature over the cross-section of the pulse tube for D= 1 mm, f= 300 Hz, and aspect ratio of 10 at the middle of pulse tube (L_{PT}/2).

Figure 7 shows the effect of various parameters and miniaturization on the efficiency of the pulse tube. The efficiency is defined in equation 11. Figure 7 (a) shows the effect of T_{cold} variation on efficiency at f= 300 Hz, and aspect ratio of 10, where T_{cold} varies from 80 K to 190 K and from 40 K to 60 K while T_{hot} remains constant at 300 K and 80 K, respectively. In all cases, as T_{cold} increases the efficiency improves. This happens because temperature gradient decreases across both sides of the pulse tube and that leads to more moderate axial variation of temperature and lower boundary layer losses.

Similar trends are observed when T_{cold} remains constant and T_{hot} is varied, as shown in Figure 7 (b). Aspect ratio and frequency are the same as those for Figure 7 (a), and T_{hot} is changing from 300 K to 190 K and from 80 K to 60 K while T_{cold} remains constant at 80 K and 40 K, respectively. Increasing

T_{hot} leads to an increase in temperature gradient and lowering of the efficiency. Once again, when T_{cold} is 40 K, much higher efficiency is achieved in comparison to the other set of simulations where T_{cold}= 80 K.

The simulations with bounding temperatures of 80K-300K show drastic reductions in efficiency as the pulse tube diameter decreases. However, this is not observed for the temperature range of 40K-80K mainly because of their smaller temperature gradients. This suggests that although at high frequencies miniaturize pulse tubes are not useful at the first stage of cryocoolers, such miniature pulse tubes can be used in the second stages of hybrid Stirling/pulse tube cryocoolers.

Figure 7 (c) and (d) examine the effects of aspect ratio and working frequency. Fixed bounding temperatures of 80K-300K and 40K-80K are applied for these cases, with an aspect ratio of 10, while the frequency is varied from 175 Hz to 300 Hz. Furthermore, the effect of aspect ratio is examined at a fixed frequency of f= 300 Hz while the aspect ratio is varied from 6 to 14. Figure 7 (c) indicates that increasing the aspect ratio improves the efficiency. Increasing the aspect ratio while the diameter is constant leads to an increase in the pulse tube length, a more moderate temperature gradient across the pulse tube, and thereby an efficiency improvement. Frequency has the least effect on the efficiency as shown in Figure 7 (d). The efficiency improves only slightly as the frequency is decreased.

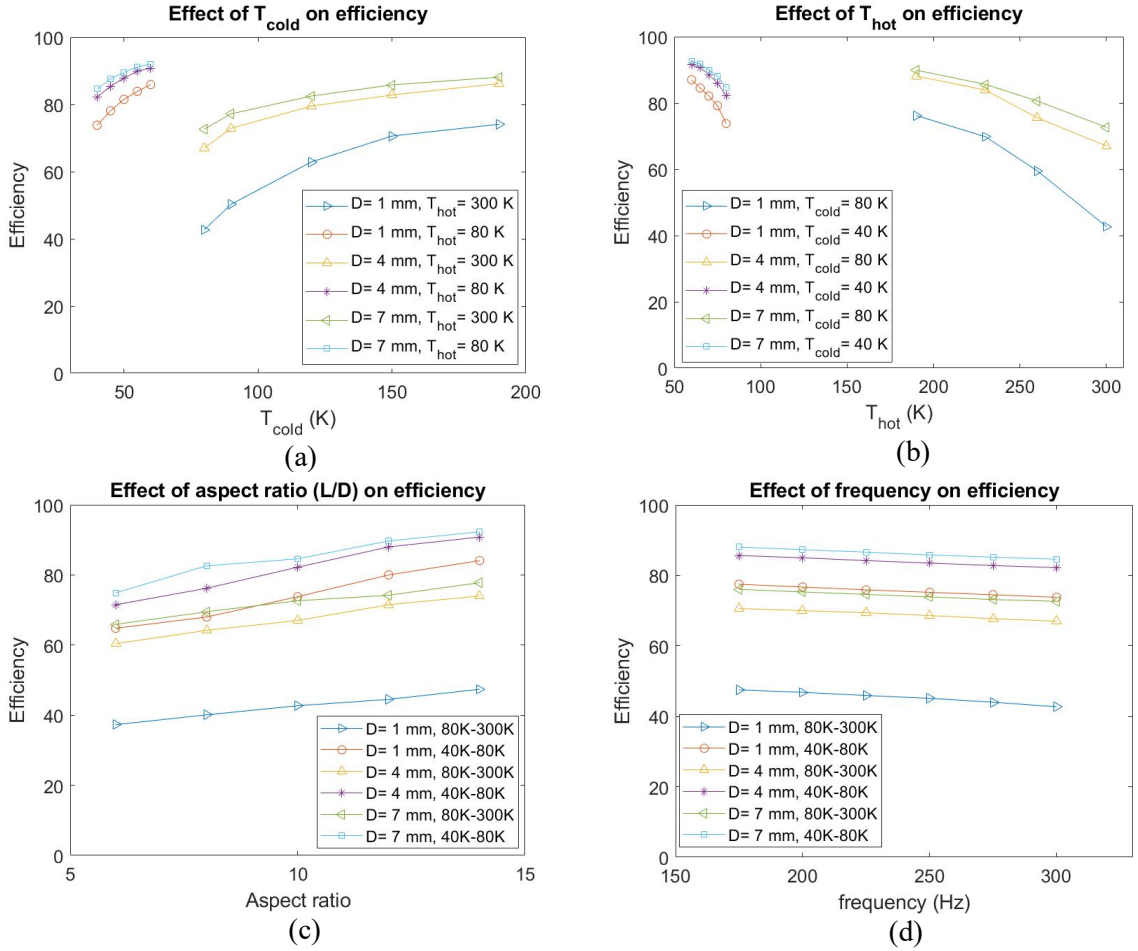

Figure 7. Effect of different parameters on pulse tube efficiency, (a) effect of cold end temperature, (b) effect of hot end temperature, (c) effect of aspect ratio, (d) effect of frequency.

6. Conclusion

A CFD-assisted study was performed as a follow-up to our previous work [3] to investigate the effects of geometric parameters and operating conditions on boundary layer losses in miniature pulse tube cryocooler. The effects of diameter, bounding (cold and warn end) temperatures, frequency and pulse tube aspect ratio on pulse tube efficiency were investigated. It was shown that, for the parameter ranges addressed in this study, the pulse tube efficiency deteriorates drastically as the diameter shrinks from 7 mm to 1 mm, particularly when the cold and warn end temperatures were equal to 80 K and 300 K, respectively. These results confirm that miniature pulse tubes are not appropriate for the first stage of miniaturized cryocoolers that function at high frequency. However, lowering the temperature gradient across the pulse tube by reducing the bounding temperatures as well as increasing the aspect ratio of the pulse tube improve the efficiency of the pulse tube, implying that miniature pulse tubes can be an appropriate option for the second stage of miniaturized cryocoolers.

7. References

[1] Willems, D., Arts, R., de Jonge, G., Mullie, J. and Benschop, T., 2016. Miniature Stirling Cryocoolers at Thales Cryogenics: Qualification Results and Integration Solutions. In *International Cryocooler Conference, Boulder* (pp. 85-93).

[2] Nast, T., Olson, J., Champagne, P., Roth, E., Saito, E., Loung, V., McCay, B., Kenton, A. and Dobbins, C., 2016. Development of Microcryocoolers for Space and Avionics Applications. In *International Cryocooler Conference, Boulder* (pp. 65-74).

[3] Kirkconnell, C., Ghavami, A., Ghiaasiaan, S.M. and Perrella, M., 2017, December. Role of size on the relative importance of fluid dynamic losses in linear cryocoolers. In *IOP Conference Series: Materials Science and Engineering* (Vol. **278**, No. 1, p. 012173). IOP Publishing.

[4] Kirkconnell, C.S., Ghavami, A. and Ghiaasiaan, S.M., 2018, June. Computational fluid dynamics study of displacer" shuttle loss" in miniature Stirling cryocoolers. In *Tri-Technology Device Refrigeration (TTDR) III* (Vol. **10626**, p. 1062604). International Society for Optics and Photonics.

[5] Kirkconnell, C.S., Hon, R.C., Perella, M.D., Crittenden, T.M. and Ghiaasiaan, S.M., 2017, May. Development of a miniature Stirling cryocooler for LWIR small satellite applications. In *Tri-Technology Device Refrigeration (TTDR) II* (Vol. **10180**, p. 1018002). International Society for Optics and Photonics.

[6] Klein, S.A. and Alvarado, F.L., 2008. EES: Engineering Equation Solver, User manual. *F-chart software*.

[7] Fluent, A., 2011. 14.5 User's Guide. *Fluent Inc., Lebanon, NH*.

[8] Schildt, H., 2003. *C++: The complete reference*. McGraw-Hill.

[9] Hunt, B.R., Lipsman, R.L. and Rosenberg, J.M., 2014. *A guide to MATLAB: for beginners and experienced users*. Cambridge university press.

[10] Tecplot, I.N.C., 2013. Tecplot 360 User's Manual Release 1.

Acknowledgments

This work was funded by West Coast Solutions through a grant to the Georgia Tech Foundation.